ANALYSIS OF THERMOCHEMICAL MODELING AND SURFACE CATALYTICITY IN SPACE VEHICLES REENTRY

A. Viviani, G. Pezzella*, C. Golia
Seconda Università di Napoli (SUN), via Roma 29, 81031 Aversa, Italy
* Centro Italiano Ricerche Aerospaziali (CIRA), via Maiorise, 81043 Capua, Italy

Keywords: *Atmospheric Reentry, Nonequilibrium Hypersonic Flow, Aerothermochemistry, Capsule-type Vehicle Aerodynamics, Thermal Shield Catalyticity.*

Abstract

A numerical study has been conducted to assess the effects of thermochemical modeling and surface catalyticity on the design of a Crew Return Vehicle reentering from Low Earth Orbit. The effects of: complexity of chemical models, kinetics of reactions, vibrational relaxation, and wall reaction mechanism on vehicle aerothermodynamics and aerodynamics, and on some flowfield features, are highlighted. Several numerical results, between perfect and non-equilibrium reacting gas approximations, are provided and compared to establish the model influence on aerodynamic performances (lift, drag, pitching moment and trim angle of attack) and aerothermodynamic performance (convective heat flux distribution on the vehicle forebody heat shield). These parameters are of primary relevance for the design of reentry trajectory and vehicle thermal protection system; for the latter, in particular, it is pointed out the role played by the surface catalyticity on the vehicle thermal load. In this framework, a possible Earth-entry scenario for the proposed capsule-type vehicle is reported and analyzed; Euler and Navier-Stokes computations have been performed, both in trajectory-based and space-based design approaches.

1 Introduction

Flight measurements, collected during reentry, have demonstrated that real gas effects can significantly influence both aerodynamics (e.g. the vehicle stability) and aerothermal loads of hypervelocity vehicles. On the other hand, trajectory calculation for atmospheric reentry involves determination of vehicle aerodynamics and aerothermodynamics. Therefore, accurate modeling of flow physics, in particular flow chemistry, is mandatory within numerical computations of reentry vehicle design. In this paper, we stress this point with an application to a capsule-type Crew Return Vehicle (CRV) as possible support servicing for the International Space Station (ISS).

However, high accuracy in modeling coupling of flow and chemistry, may result only in a poor increase of accuracy of numerical results, despite the high modeling efforts and the increased computational cost. So, one must balance the theoretical and computer time effort needed to use a more general and sophisticated model against the expected accuracy of the numerical results. Then, the question arises to which extent number of reactions, coefficients, reaction mechanism, etc. influence the flow.

To answer this question, a step-by-step numerical investigation has been carried out. Indeed, several simulations have been performed to examine the influence of the chemical reactions, its mechanisms and kinetics, and thermal nonequilibrium on aerodynamic and aeroheating of a capsule-shaped reentry vehicle, in the framework of a Low Earth Orbit (LEO) mission scenario. Two-dimensional axisymmetric and three-dimensional Euler and Navier-Stokes computations are performed, for perfect gas and reacting gas mixture, in thermal and chemical nonequilibrium, to examine the air flows around the capsule, for several chemical reaction mechanisms.

In particular, viscous simulations are computed with different wall-surface boundary conditions: non catalytic wall (NCW), partially catalytic wall (PCW), fully catalytic wall (FCW), to underline the effect of the heat shield catalyticity on the aerodynamic heating.

The work confirms that high-temperature transport phenomena markedly influence the vehicle flowfield and, in turn, the vehicle aerodynamics and aerothermodynamics, but it also stress that, with an acceptable loss of results accuracy, we do not need to use models of so high complexity, thus saving much computing time.

2 Flow and Chemistry Coupling in Reentry Hypersonic Flight

During atmospheric descent, reentry vehicles encounter several flow regimes and thermochemical phenomena: they fly from free molecular to fully continuum phases and, when in continuum, from laminar to fully turbulent flows. Due to the high free-stream enthalpy, chemical effects come in, since the bow shock is strength enough to generate a several species reacting mixture flow around the vehicle. For instance, when flow velocity is low, energy is absorbed only into particles vibration and rotation degrees of freedom (dof).

But as velocity increases enough, the thermal energy of the gas becomes comparable with the energy associated with a whole range of gas phase chemical processes, such as the excitation of molecular modes of vibration; the dissociation of oxygen and nitrogen; the formation of other chemical species through recombination reactions; the ionisation of both molecular and atomic species.

As a consequence, the flowfield chemical composition around the reentry vehicle varies spatially and temporally and, because shock layer molecules continuously exchange its energy between the translational and internal dof, the air can result in a thermal-and/or chemical nonequilibrium mixture. Of course this scenario emphasizes depending on the kind of reentry (i.e. orbital or superorbital one).

Therefore, the accurate numerical simulation of reentry flows can be very challenging, depending on the more or less correct and accurate modelling of the thermo-chemical processes.

Generally speaking, the mathematical model describing the flowfield physics around an hypervelocity vehicle deals with balance equations for a multispecies chemically reacting gas mixture supplemented with an appropriate set of chemical reactions (i.e. the reactions mechanism) and with equations modelling species vibrations relaxation (i.e. thermal non-equilibrium).

In particular, the number of chemical species and number of reactions to consider as relevant depend on the vehicle trajectory. For example, numerical computation of a flowfield involving ionized species, as for superorbital reentries, demands at least 11 chemical species with 20 reactions, whereas for lower velocity reentries, 5 non-ionized species and 17 reactions are sufficient.

Simulation problems may arise because the coupling of flow and chemistry leads to a stiff problem due to differences in reaction rate characteristic times [1,2]; dissociation rate coefficients can differ by orders of magnitude and, since reaction rates are very difficult to be measured, different values may exist for the same coefficient. Therefore, the appropriate set of reactions, to be used in a given application, represents a very relevant choice.

Such a choice is still more relevant because, in general, increasing model complexity does not equivale to increasing accuracy of numerical results, despite the higher computational cost needed for increased reaction set. Moreover, when one increases the number of chemical reactions, numerical results can be much influenced by the effect of the uncertainty in input data, such as species transport coefficients, relaxation times for thermal and chemical non-equilibrium.

So, it could be important to simplify the reaction mechanisms, by reducing as much as possible the number of chemical reactions, without loss in accuracy but greatly reducing computing time. Among the most simple reaction mechanisms, currently in use, there is the set of three reactions, named Zeldovich process [1], summarized in paragraph 6.2.

The reactions considered above, taking place only in the gas phase, are termed homogeneous chemical reactions. They differ from the heterogeneous reactions that, instead, occur near the vehicle wall involving gas and solid species. Heterogeneous reactions describe recombination of flowfield atomic species that were formed by gas dissociated through the bow shock. They can be catalyzed by the thermal protection material (TPM) and, being exothermic, contribute to the aeroheating of the vehicle. Thus, the TPM, promoting or preventing species recombination at wall, depending on its catalyticity, plays an important role in the aerodynamic heating, as explained in the next paragraph.

3 Real Gas Aerothermodynamics within LEO Reentry Missions

The shock wave produced ahead of the reentry vehicle, when travelling at hypersonic speed, suddenly elevates the temperature of the surrounding air, especially around the nose where the shock is more intense: thermal and chemical characteristics of the gas in the shock layer are altered in such a way that depends on the atomic and molecular structure of the air species [3]. Hence, the microscopic structure of the mixture species, affecting the ways in which energy may be redistributed, influences the specific heat ratio (γ), the chemical reaction rates, and the transport properties. These quantities, in turn, affect the dynamics of the flow and the character of shock and expansion waves (i.e. pressure, temperature, and velocity distributions), the chemical energy diffused to the surface (i.e. the chemical contribution to the heat flux at the wall), the boundary layer structure (i.e. the heat flux and shear stress).

In particular, the flow chemical dissociation results in a large density ratio (ε) across the strong bow shock, on which the aerodynamics of capsules markedly depends. In fact, the change of aerodynamic characteristics are the result of change in wall-surface pressure due to changes, influenced by ε, of shock shape and stand-off distance. The surface pressures are affected by a change in shock density ratio,

because the pressure level, at the stagnation point (e.g. Cp_{max}), is changed:

$$C_{p\max} = C_{pt2} = \frac{P_{t2} - P_\infty}{q_\infty} = \left(\frac{P_{t2}}{P_\infty} - 1\right)\frac{2}{\gamma M_\infty^2} \cong 2 - \varepsilon \quad (1)$$

where ε, in the hypersonic limit reads:

$$\varepsilon = \lim_{M_\infty \to \infty} \frac{\rho_1}{\rho_2} = \frac{\gamma - 1}{\gamma + 1} \quad (2)$$

Moreover, high temperature effects also modify the hypersonic capsule-vehicle aerodynamics and aerothermodynamics by means of a very abrupt change in the capsule trim angle of attack. This is due to the shift of the sonic line position at the vehicle leeside because of the change in (γ), thus affecting the capsule pitching moment coefficient, C_{MY} (capsule static aerodynamic stability). Note that body stability is a critical requirement for a reentry vehicle, because static instability could lead to catastrophic failure in case the thermal shield is not protecting anymore the vehicle.

Real gas effects influence also vehicle aeroheating. For instance, the thermal protection material (TPM) could promote the chemical recombination at wall of flowfield atomic species and may increase the overall heat flux up to two times or more than the value of a non-catalytic wall [1, 4, 5, 6]. Neglecting conduction into the heatshield and radiation from the gas, the energy balance at vehicle surface reads:

$$-\dot{q}_r = -\sigma \varepsilon T_w^4 = \lambda_{tr}\left(\frac{\partial T}{\partial n}\right)_w + \sum_{i=1}^{N_v}\lambda_{v,i}\left(\frac{\partial T_{v,i}}{\partial n}\right)_w +$$
$$+ \rho\sum_{i=1}^{N_S}\left(\int_{T_o}^{T} C_{Pi}\, dT + \Delta h_{fi}^o\right)D_i\left(\frac{\partial Y_i}{\partial n}\right)_w \quad (3)$$

The first term, on the right-hand side, is the conductive heat-flux, the second one is the vibrational contribution, and the last one is the species diffusion contribution, that strongly depends on the catalytic properties of TPS: the heatshield should be a poor catalyst [6,7].

4 CRV Concept and Mission Requirement

The reentry system is a scaled-up Apollo capsule measuring about 5 [m] in diameter, with a nose radius of 6.05 [m]; the sidewall angle is

33° [deg] and the overall vehicle height 3.8 [m]. The offset centre of gravity (cg) is located at x/D = 0.26 and y/D = -0.0353.
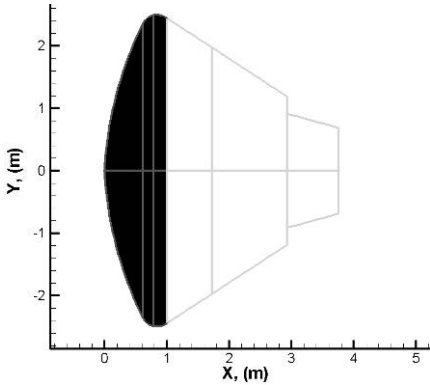

Figure 1. Vehicle configuration with quotes.

To generate an Earth entry environment, a vehicle mass equal to about 9 ton is adopted; starting from the atmospheric entry interface (h_E=120 [km]) with V_E=8 [km/s] inertial, and θ_E=-2° [deg], the reentry flight scenario is given in the Mach-Reynolds plane of Figure 2.
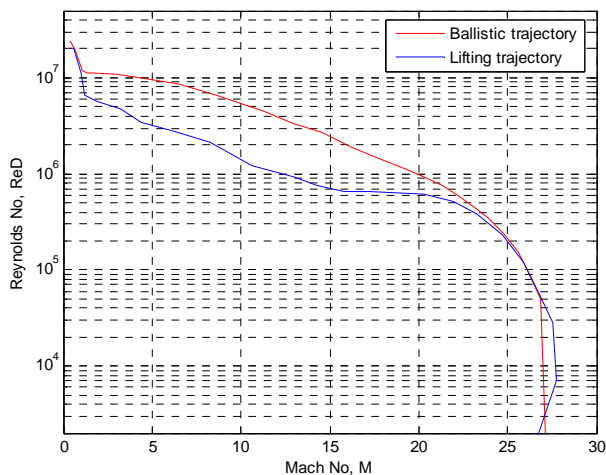

Figure 2. Reentry flight scenario, starting from LEO orbit

The red curve is a ballistic reentry trajectory and represents the worst-case from the convective heat flux point of view. Along the blue curve the capsule is flying trimmed at an AoA of 20° [deg], constant over the critical heating regime (i.e. lifting return). In Figure 3, the profile of the trim angle of attack (AoA) is provided [8].
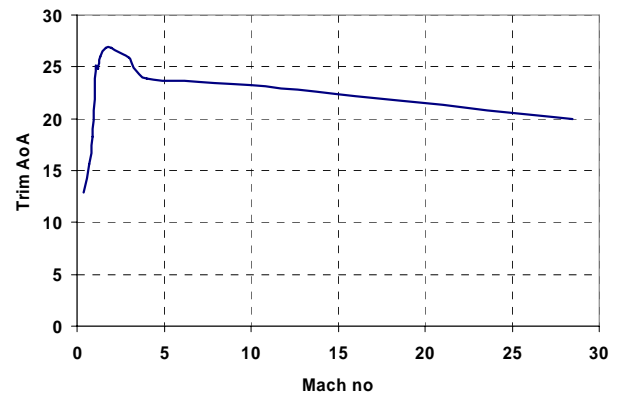

Figure 3. Trim angle of attack versus Mach number

The analysis of the entry from ISS orbit was performed by using the ENTRY (ENtry TRajectrY) code developed at SUN. Reentry trajectories result in an aerothermodynamic environment that must be accurately predicted for a reliable TPS design. To this scope, the trajectories freestream flight conditions have been used to perform numerical computations, as reported hereinafter.

5 Design Approaches and Numerical Tools

The preliminary AErodynamic DataBase (AEDB) of the CRV has been provided according to the "space-based" design approach, which dictates the generation of data set as function of a number of independent parameters (i.e. M_∞, Re_∞, α, β) [9]. On the other hand, the preliminary AeroThermodynamic DataBase (ATDB) has been computed following the "trajectory-based" design approach, which consists to perform aerothermal computations at a finite number of "critical" points of the nominal design trajectory [10, 11].

Computational analyses of the CRV flowfields are performed by means of several User Defined Functions (UDF), developed by the authors, which incorporate as core solver the code Fluent. With such UDF, the Fluent core can manage, e.g., vibrational relaxation, many catalyticity models, radiative equilibrium at the wall and other boundary conditions, etc.
Computations have been carried out on multiblock structured grids generated with the help of ICEM-CFD tool. A close-up view of 2-D axisymmetric and 3-D mesh on vehicle surface can be seen in Ref. [12]. The grid used

for 3D calculations consists of 32 blocks for an overall number of 450.000 cells. For each case, a new grid has been created to properly accommodate for the detached bow shock location. The distribution of surface grid points was dictated by the level of resolution desired in various areas of vehicle, such as stagnation region and base fillet, according to the computational scopes; see Ref. [12] for further details on the multiblock computational grids.

6 The Model and the Numerical Technique

The full set of equations for a laminar viscous hypersonic continuum flow in thermal and chemical non-equilibrium, assuming the air as a mixture of N_S perfect gases species and N_v vibrating species, can be written, with the usual meaning of the symbols (see [6, 7, 12, 13] for an extensive treatment), as follows:

Continuity:

$$\frac{\partial \rho}{\partial t} + \vec{\nabla} \cdot \left(\rho \vec{V} \right) = 0 \tag{4}$$

Momentum:

$$\frac{\partial \left(\rho \vec{V} \right)}{\partial t} + \vec{\nabla} \cdot \left(\rho \vec{V} \vec{V} \right) + \vec{\nabla} p = 2\vec{\nabla} \cdot \left[\mu \left(\vec{\nabla} \vec{V} \right)_o^s \right] \tag{5}$$

Energy:

$$\frac{\partial \left(\rho e \right)}{\partial t} + \vec{\nabla} \cdot \left[\left(\rho e + p \right) \vec{V} \right] =$$

$$= \vec{\nabla} \cdot \left[\lambda \nabla T + 2\mu \left(\vec{\nabla} \vec{V} \right)_o^s \cdot \vec{V} + \sum_i h_i \vec{J}_i \right] - \tag{6}$$

$$- \sum_i h_i \dot{\omega}_i - \sum_j \dot{e}_{vj}$$

Species:

$$\frac{\partial \left(\rho Y_i \right)}{\partial t} + \vec{\nabla} \cdot \left(\rho \vec{V} Y_i \right) + \vec{\nabla} \cdot \vec{J}_i = \dot{\omega}_i \tag{7}$$

Vibrational energy:

$$\frac{\partial \left(\rho e_{vj} \right)}{\partial t} + \vec{\nabla} \cdot \left(\rho \vec{V} e_{vj} \right) = \dot{e}_{vj} \tag{8}$$

For each species the perfect gas model applies and the Dalton's law is applicable:

$$p = \sum_i p_i \tag{9}$$

where p_i is the partial pressure of the ith species of the mixture. As a consequence, the following relation for density holds:

$$\rho = \frac{p}{R_0 T \sum_i Y_i / M_i} \tag{10}$$

where R_0 is the universal gas constant. The internal energy of the mixture is defined as:

$$e = \sum_i \left(Y_i e_i \right) \tag{11}$$

where e_i, the internal energy of the single component gas, is the sum of the energies representing the different degrees of freedom of the molecules. Finally, the enthalpy is:

$$h = \sum_i \left(Y_i h_i \right) \tag{12}$$

Computation of the diffusive fluxes requires knowledge of the transport coefficient.

6.1 Transport properties

For pure species, the following expressions are derived from kinetic theory of gases [6, 7, 12]:

Viscosity:

$$\mu_i = \frac{2.6693 \times 10^{-6} \sqrt{M_i T}}{\sigma_i^2 \Omega_{\mu i}} \tag{13}$$

Thermal conductivity:

$$\lambda_i = \frac{15}{4} \left(\frac{\mu_i R_0}{M_i} \right) \left(\frac{4}{15} \frac{c_{pi} M_i}{R_0} + \frac{1}{3} \right) \tag{14}$$

Mass diffusivity:

$$D_{ij} = \frac{0.0188 \times T^{\frac{3}{2}} \sqrt{\left(M_i + M_j \right) / M_i M_j}}{p \sigma_{ij}^2 \Omega_{Dij}} \tag{15}$$

where χ_i is the mole fraction of ith specie and a_i is equal to μ_i or λ_i . For the diffusion coefficient of the ith species in the mixture:

$$D_i = \frac{(1-\chi_i)}{\sum\limits_j \dfrac{\chi_i}{D_{i,j}}} \qquad (16)$$

Finally, vibrational relaxation is modelled using a Landau-Teller formulation, where relaxation times are obtained from Millikan and White, assuming simple harmonic oscillators [6,7].

6.2 Chemical species and reactions mechanism

The chemically active species of much relevance in dissociated air are N_2, O_2, N, O, NO. These species can be supplemented with ionized ones as flow energy becomes higher and higher. Therefore, within a LEO reentry scenario (no flowfield ionization occurs), the gas is approximated as a finite-rate chemistry mixture of the above species [6, 7, 12, 13].

The elementary reactions mechanism, governing the species in high-temperature air, deals with three dissociation reactions and two exchange reactions, as reported in Tables 1a, 1b; there M, namely reacting partner or third body, can be any of the five reacting species, thus providing or removing collision energy. Efficiencies of the third body are also reported in Tables 1a, 1b, since they are employed in computations to increase CPU time efficiency. Hence, the reactions mechanism results in a system of 17 chemical reactions, with 17 forward and backward reactions rate coefficients.

Among the simpler sets of homogeneous reactions, it is standard to use the following set of only three chemical reactions, known as Zeldovich process [1]:

$$O_2 + N_2 = 2O + N_2$$
$$N_2 + O = NO + N \qquad (17)$$
$$NO + O = O_2 + N$$
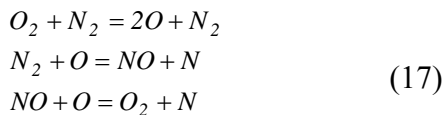
It considers only oxygen dissociation, due to collisions with molecular nitrogen, and two exchange reactions. This model can be explained considering that the gas is so hot that the oxygen dissociates nearly completely, while the nitrogen does not dissociates completely and

fast as the oxygen. Finally, exchange reactions are important because they determine the speed of nitrogen dissociation.

Chemical reactions proceed with forward (f) rates, $k_{f,r}$ that appear in the source terms ($\dot{\omega}_i$) of the species transport equation, Eq. (7). The rates $k_{f,r}$ are expressed in the Arrhenius form as:

$$k_{f,r} = k_{f,r}(\overline{T}) =$$

$$= A_{f,r} \overline{T}^{\beta_{f,r}} \exp\left(-\frac{E_{a_{f,r}}}{R_o \overline{T}}\right) \qquad (18)$$

where $\overline{T}$ and the constants depend on the model kinetics (see Tables 1a, 1b).
Dunn-Kang model uses only one temperature to describe all the energy modes ($\overline{T} = T$, thermal equilibrium), whereas Park model assumes that the temperature $\overline{T}$ can be T, T_v, or $T^a T_v^b$ (namely rate controlling temperature) depending on the reaction (see Table 1b); as well known, Park's two-temperature model, accounting for both T and T_v provides more accurate results. In fact, Park uses T to describe translational and rotational energy modes and T_v for vibrational and electron-translational modes [13,14,15].

6.3 Boundary conditions

Eq. (3) states that the properties of a surface are represented by emissivity (ε) and wall catalyticity (i.e. k_{wi}). Since atoms produced by dissociation reactions strike the surface, the catalyticity property of the wall is implemented by means of a production term (i.e. $\dot{\omega}_{wi} \neq 0$) for the boundary layer problem to solve. Indeed, steady-state mass atomic conservation at the wall states that the production of ith species, due to the catalytic recombination rate, must be balanced by the rate of diffusion to the surface:

$$\dot{\omega}_{wi} = k_{wi}(\rho_w Y_{wi})^\delta = \left(\rho D_i \frac{\partial Y_i}{\partial n}\right)_w \qquad (19)$$

where δ is the reaction order and k_{wi} is the catalytic reaction rate [6].
When the TPM does not promote any particular reaction (i.e. $\dot{\omega}_{wi} = 0$), the TPS surface refers as

NCW (i.e. $k_{wi}=0$); on the opposite situation, when the TPM can activate any reactions, the TPS surface is called FCW (i.e. $k_{wi} \rightarrow \infty$). Between these two limit cases (i.e. $0 < k_{wi} < \infty$), the vehicle surface is considered as PCW and the heat fluxes to the vehicle can greatly differ depending on the value of k_{wi}. Furthermore, when a low conductive TPS protects the vehicle, the radiative equilibrium holds at vehicle surface; to account for this condition, during numerical simulations, the wall temperature is calculated by Stephan-Boltzman law and is updated at each streamwise station by means of a Newton-Raphson approach, that usually achieves convergence within few iterations.

6.4 Numerical technique

The governing equations, together with the proper boundary conditions, are discretized using a cell centered finite volume formulation on a structured multi-block grid. The inviscid fluxes at cell interfaces are calculated by using a Flux Difference Splitting (FDS) Riemann solver, since upwind methods are particularly suitable for high speed flows. However, second order accuracy is not automatically reached; for this reason, a second order ENO (Essentially Non Oscillatory) technique for the reconstruction of cell interface values is employed [16,17]. The viscous fluxes are calculated by central differencing, i.e. computing the gradients of flow variables at cell interfaces by means of Gauss theorem. The method is second order accurate in space. Time integration is performed by employing both an explicit single-stage (Euler forward) algorithm and an explicit five stage Runge-Kutta scheme, coupled with an implicit evaluation of the chemical and vibrational source terms, under the hypothesis of time marching approach to reach the steady solution for the flow.

7 Reliability of Numerical Study

In order to assess reliability of numerical results of the present design environment, a rebuilding of ONERA S4 wind tunnel (WT) tests, reported in Ref.18, has been performed.

The S4 test campaigns provide pressure profiles on the forebody centerline of the Atmospheric Reentry Demonstrator (ARD) capsule, developed by ESA. This experimental test campaign has been chosen as benchmark being ARD an Apollo-shaped capsule too.
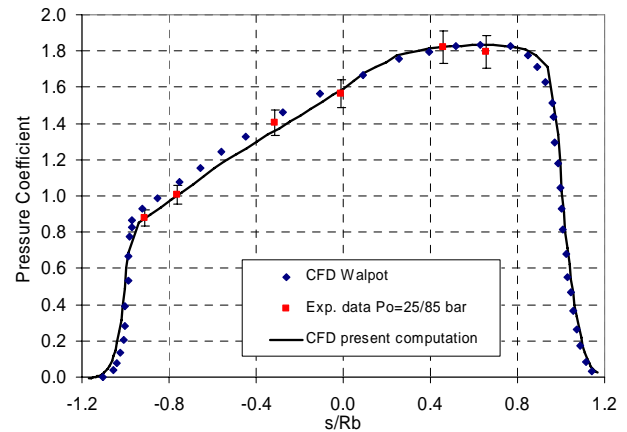

Figure 4. Pressure coefficient on forebody centerline. Comparison between present computation and data provided in [18].
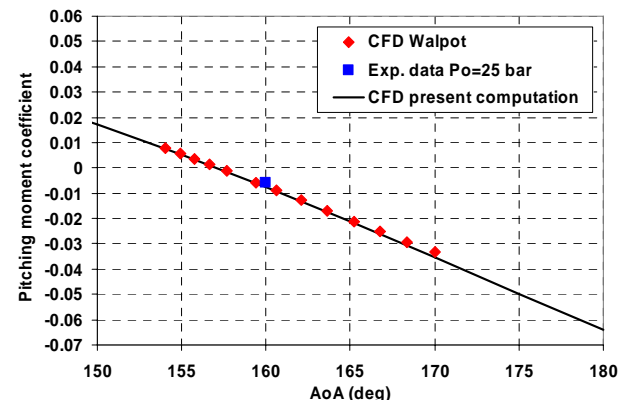

Figure 5. Pitching moment coefficient. Comparison between present computation and data provided in [18].

Test freestream conditions are summarized in Tab. 2. They refer to S4 exit conditions for two different Reynolds number, at a Mach number of about 10. Pitching moment versus AoA is also provided.

Recalling that experimental tests were performed with a flow total temperature of about 1100 [K], numerical CFD simulations are performed with perfect gas model only. Results of present computations are summarized and compared with experimental data in Figs. 4-5, where are also reported CFD data provided by Walpot, as further benchmark [18]. As one can

see, Figures 4-5 highlight that experimental and numerical data compare well, thus confirming reliability of numerical results of the present design environment. Evidences of UDF capabilities with Fluent core solver to simulate flowfield features in reacting gas conditions, as performed by authors, can be found in [12].

8 Computational Analysis of CRV Flowfield

Axisymmetric and fully three-dimensional simulations were performed at the freestream conditions listed in Table 3, with the farfield composed by 79% nitrogen (N_2) and 21% oxygen (O_2). Solutions are 2nd order scheme accurate in space as highlighted by the sharped line of contours.

In order to appreciate how vehicle flowfield depends on real gas effects, numerical computations are performed in a step-by-step approach, starting with perfect gas model, hence chemistry come in by considering first the flow in equilibrium conditions and then in non-equilibrium. In the latter case, the effects of both reactions mechanism and chemical kinetics are considered, as for example by means of Zeldovich reactions mechanism and Dunn-Kang and Park kinetic models. Finally, thermal non-equilibrium and wall catalyticity are accounted for, providing a complete overview of high temperature effects on CRV flowfield.

8.1 Axisymmetric computations

The results to be shown refer the investigation of the peak heating point of the ballistic trajectory of Fig. 2.

A general overview of the flowfield past the vehicle is shown in Figures 6-7, where contours of pressure and translational temperature in the forebody flowfield are plotted, respectively. These contours refer to M_∞=19, H=57 km and AoA=0 deg, in the case of perfect gas computation.

Figure 8 shows the non-dimensional temperature profile comparison between perfect gas (PG), equilibrium gas (EG), chemical non-equilibrium gas with NCW and chemical non-equilibrium gas with FCW, as evaluated along the stagnation line.
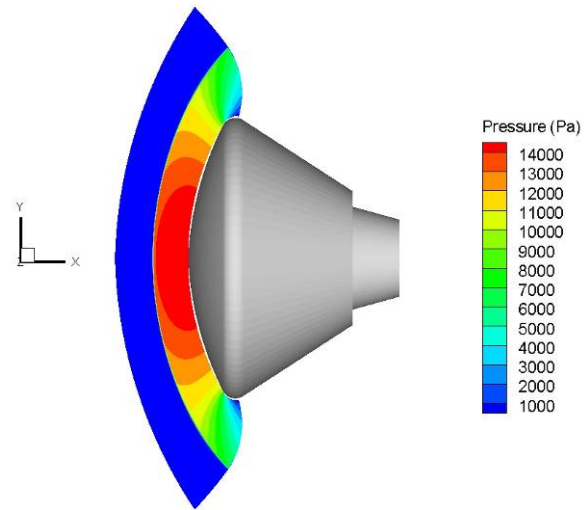

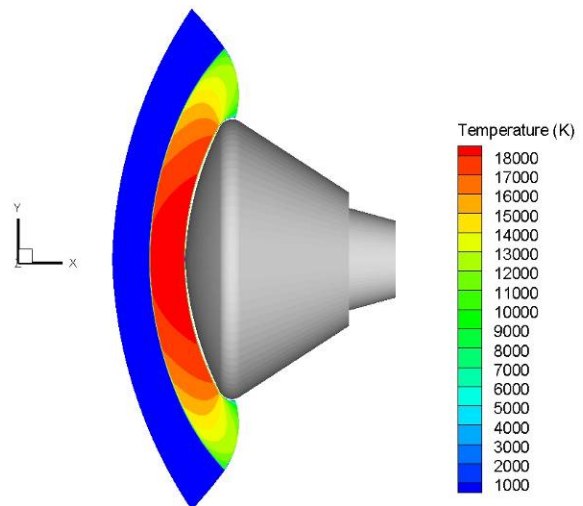**Figure 6.** Contours of static pressure for AoA=0 deg, M_∞=19, and H=57 km. Perfect gas computation.

Figure 7. Contours of static temperature for AoA=0 deg, M_∞=19, and H=57 km. Perfect gas computation.

As clearly shown, the temperature is large enough to cause the complete oxygen dissociation in the shock layer while nitrogen partially dissociates. Moreover, differences can be found on temperature peak, stand-off distance and also on the equilibration trend for translational temperature.

In particular, in the case of chemical non-equilibrium computation, the temperature profile on the stagnation line exhibits a sharp discontinuity at the shock wave and a large overshooting value due to the finite rate dissociation of molecules.

Figure 8 also shows that the shock layer become thinner because high temperature phenomena absorb heat, thus decreasing the effective specific heat ratio γ.
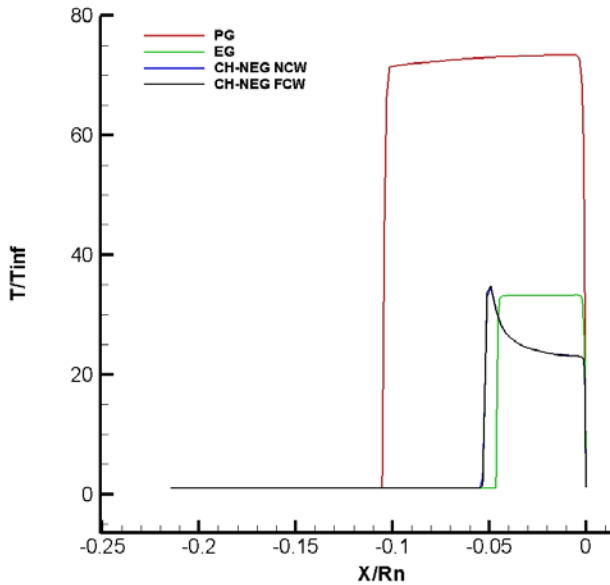

Figure 8. Comparison of static temperature for AoA=0 deg, M_∞=19, and H=57 km, along stagnation line.
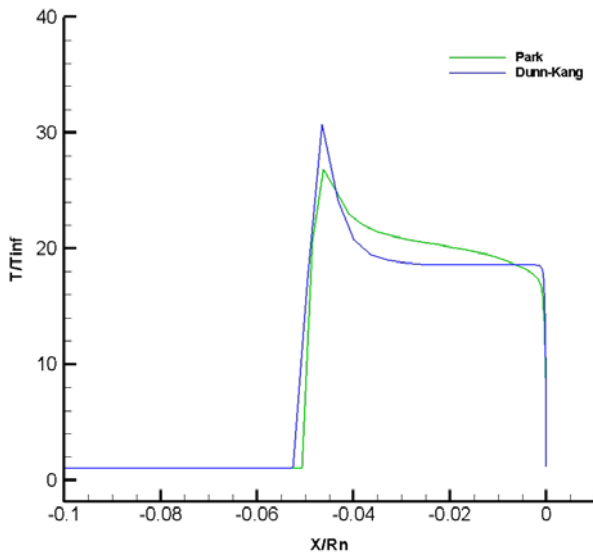

Figure 9. Comparison of translational temperature along the stagnation line for different chemical models.

As a result, the gas compressibility changes, which leads to changes in the shapes of shock waves around the vehicle. In particular, as green curve highlights, this phenomenon occurs more prominently in the equilibrium flow than in a non-equilibrium one.

If we account for the influence of chemical kinetics, in Figure 9 the comparison of non-dimensional temperature profiles along the stagnation line between results for Dunn-Kang e Park models has been provided.

As shown, chemical kinetics slightly changes both stand-off distance and the peak temperature. Differences are also in the shape of temperature profiles in the shock layer, considering that, for Dunn-Kang model, the flow equilibrates before reaching boundary layer as for the case of Park model.

The effect of vibrational relaxation can be appreciated in Figure 10, where comparison between translational temperature distributions, along the stagnation line, is reported for Park kinetics.
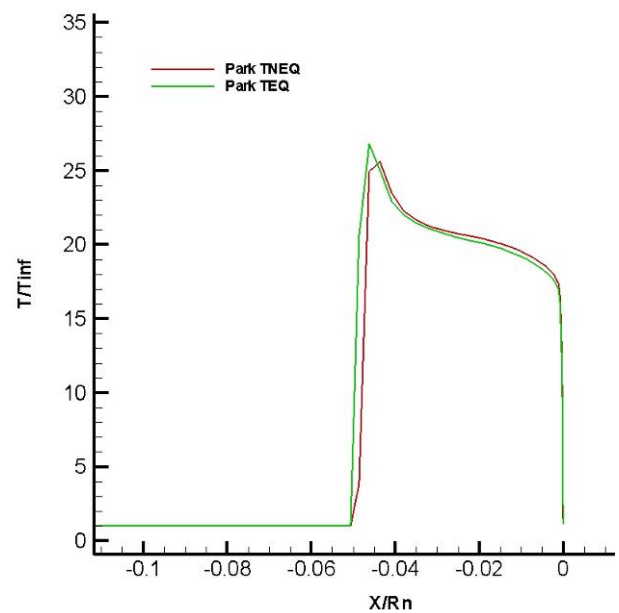
Figure 10. Translational temperature along the stagnation line. Comparison between thermal equilibrium and nonequilibrium conditions. Park kinetics.

Results remark only slight differences between the case of thermal equilibrium and non-equilibrium computation. When vibrational equilibrium holds (green curve) there is no incubation time for vibration to relax, as highlighted by temperature rise of the curve. Therefore, we can conclude that at the peak heating the flowfield around the capsule is characterized by quite thermal equilibrium conditions (remember that capsule features a large forebody radius, R_N=6.05 m).

Hence, chemistry is active just behind the shock and energy goes only in chemistry thus yielding lower translational temperature in the shock layer. In fact, even if the exact functional dependence is unknown, it is agreed that a reaction mechanism depending only on T over-predicts the amount of dissociation [19].
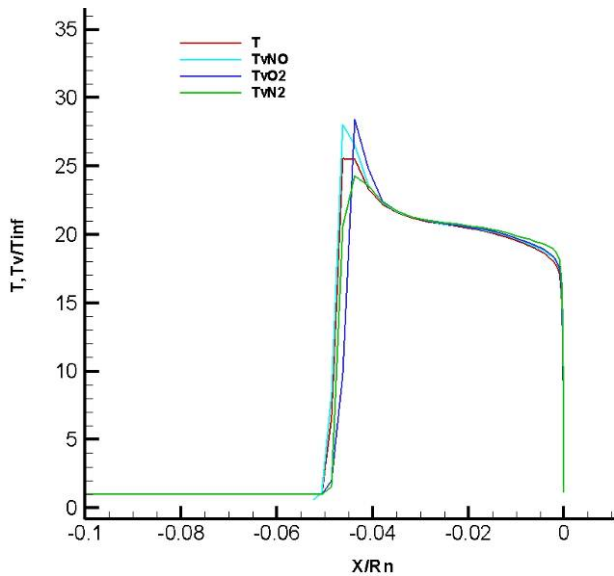

Figure 11. Comparison of translational and vibrational temperatures for AoA=0 deg, M_∞=19, and H=57 km, along stagnation line for NCW.

Thermal equilibrium conditions are also confirmed by results summarized in Figure11, where comparison of translational and vibrational non-dimensional temperatures is reported. As we can see, the temperature profiles are almost overlapped except across the shock, with the vibrational temperature of molecular nitrogen that slightly lags behind the others (the energy transfer takes a certain number of collisions to proceed); in particular, O_2, NO and N_2 quickly equilibrate.

For what concerns the effects of reactions mechanism, Figure 12 reports the same evaluations as in Figure 9, but in the case of Zeldovich reactions mechanism. As shown by numerical results, the Zeldovich reactions mechanism over-estimates both temperature peak and stand-off distance. In particular, the temperature profile of complete reactions mechanism (blue curve), shows that flowfield in the shock layer tends toward equilibrium faster than Park and Zeldovich results.
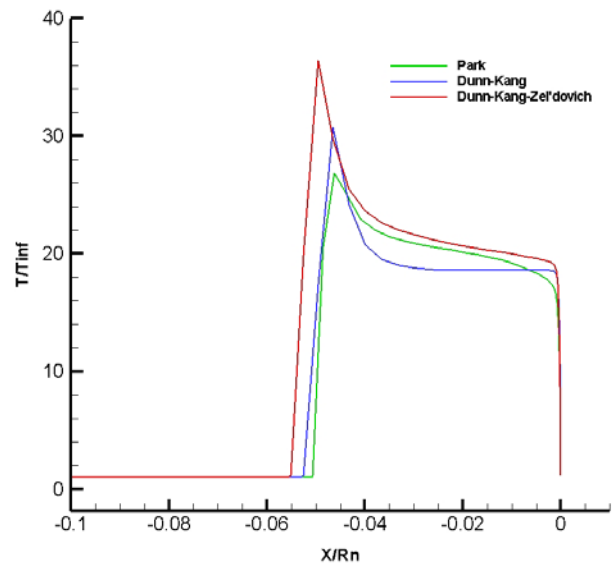

Figure 12. Translational and vibrational temperatures for AoA=0 deg, M_∞=19 and H=57 km. Comparison along stagnation line for complete reaction system and Zeldovich model.

8.2 Three-dimensional computations

In the framework of 3-D computations, four AoA have been considered (i.e. 10, 17.5, 21, 28 deg). Figure 13 reports the flowfield contours of oxygen mass fraction with streamtraces for M_∞=19, H=57 km, and AoA=10 deg.

As expected, the oxygen is fully dissociated. Figure 14 shows Mach number flowfield contours and streamtraces around CRV flying at AoA=21 deg, M_∞=19 at an altitude of 57 km.

Contours of pressure (Pa) on capsule pitch plane and forebody, when vehicle is flying at AoA=28 deg, are recognized in Figs. 15-16, respectively. As one can see, CFD flowfield computations show that, at the shoulder, the flow turns and expands rapidly. The boundary layer detaches, forming a free shear layer that separates and, as highlighted by streamtraces, the wake flow evolves in a highly asymmetric way with the separation bubble confined to the leeward side of the capsule.

Concerning capsule static stability, the transition in sonic line location is shown in Figures 17-21 for different AoA and Mach numbers. Figure 17 reports sonic line location for four cases, involving two different Mach numbers (10 and 19) and all the AoA considered in the computations.
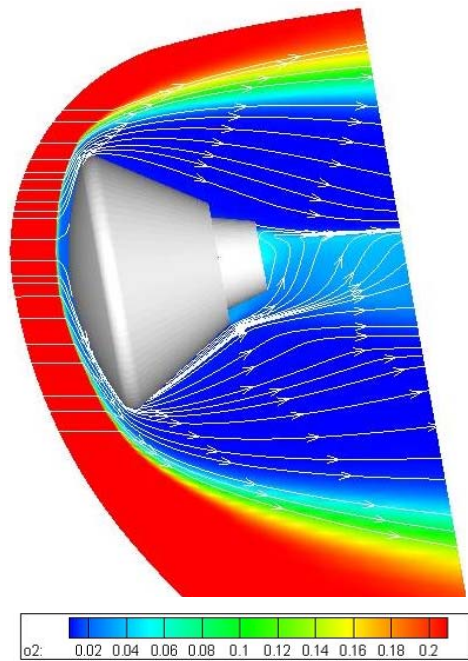
Figure 13. Contours of oxygen mass fraction with streamtraces for AoA=10 deg, M_∞=19, and H=57 km. Reacting gas computation.
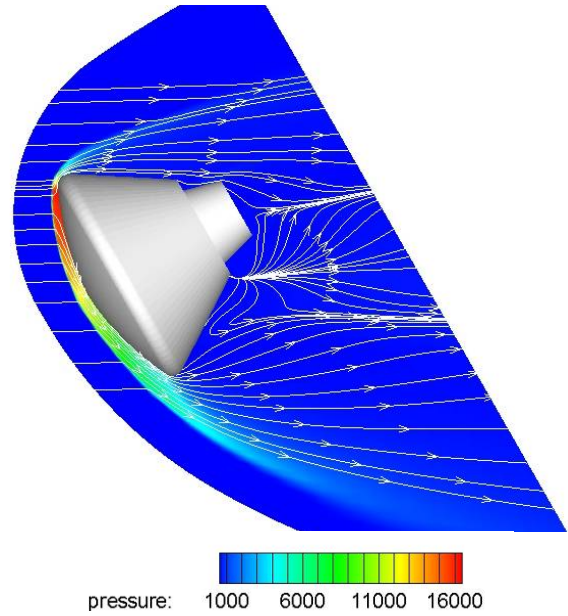

Figure15. Contours of pressure flowfield (Pa) with streamtraces for AoA=28 deg, M_∞=19 and H=57 km. Reacting gas computation.
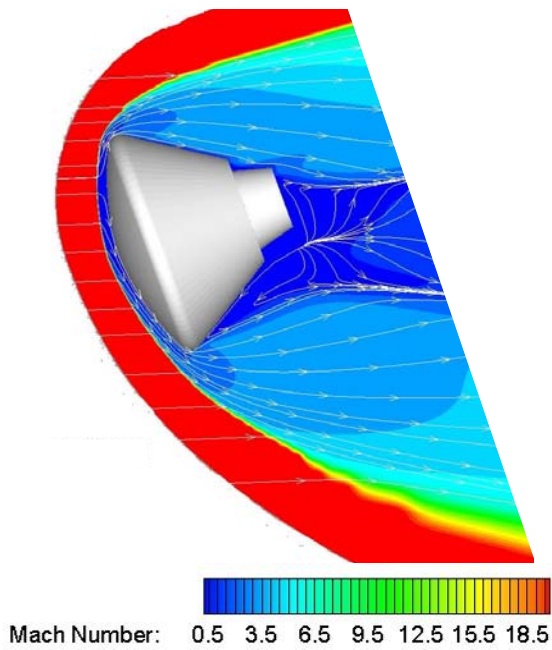

Figure 14. Contours of Mach number flowfield with streamtraces for AoA=21 deg, M_∞=19, and H=57 km. Reacting gas computation.
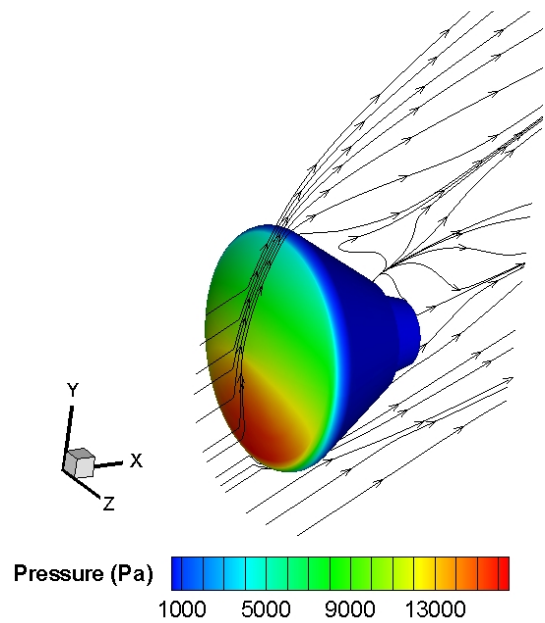

Figure 16. Contours of pressure distribution (Pa) on capsule surface at AoA=28 deg with streamtraces for M_∞=19 and H=57 km. Reacting gas computations.

As one can see, the sonic line location and its shape markedly depend on freestream mach number, altitude and AoA, thus highlighting that capsule attitude conditions are highly influenced during descent flight.
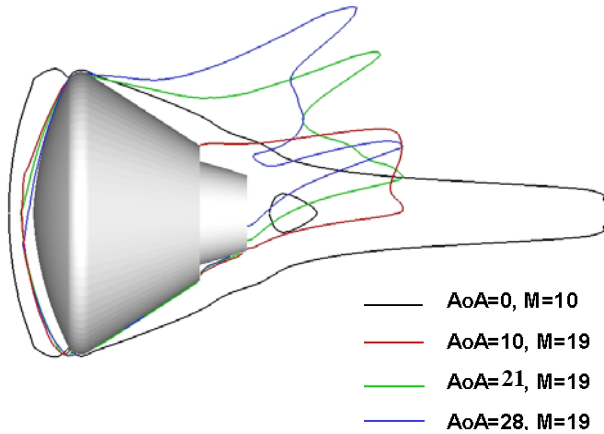

Figure 17. Sonic line location in the capsule pitch plane for different AoA (i.e. 0, 10, 21, and 28 deg) and Mach number (i.e. 10 and 19). Reacting gas computations.
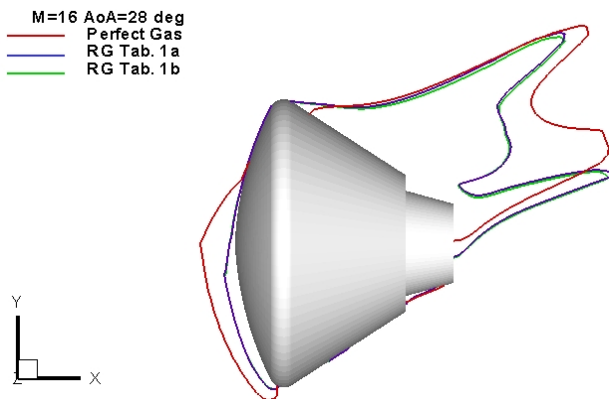

Figure 18. Sonic line location in the capsule pitch plane at AoA=28 deg (i.e. 152 deg). Comparison between PG and RG computations for M_∞=16 at H_∞=57 km.

In order to appreciate the effect of finite rate chemistry, the sonic line comparison between PG and RG computations both for M_∞=16 and M_∞=19 is summarized in Figures 18 and 19, respectively.

In both cases it is highlighted that for the PG solution the flowfield around almost all the capsule heat shield is entirely subsonic with consequent high pressure distribution.
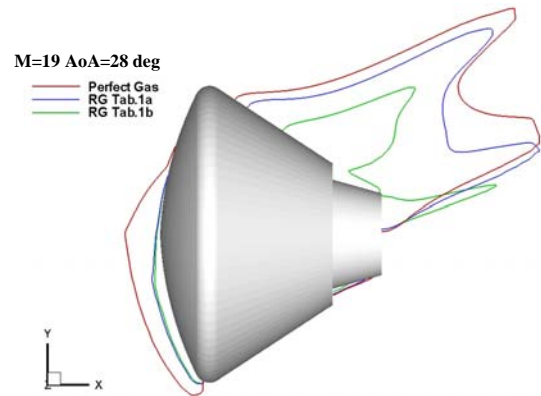

Figure 19. Sonic line location in the capsule pitch plane at AoA=28 deg (i.e. 152 deg). Comparison between PG and RG computations for M_∞=19 at H_∞=57 km.

Therefore, as sonic line shifts, due to the chemical reactions, the flow becomes entirely supersonic and the pressure decreases, confirming that pitching moment and trim AoA are affected by high temperature real gas effects.
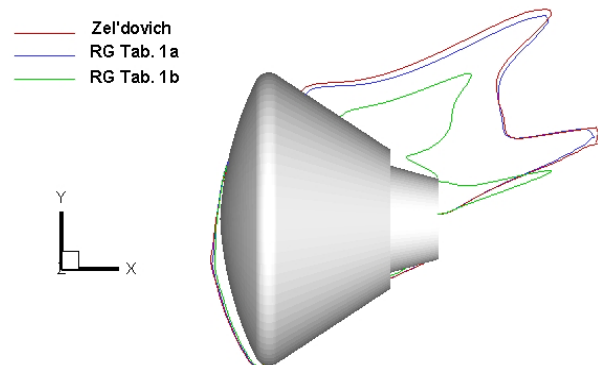

Figure 20. Sonic line location in the capsule pitch plane at AoA=28 deg (i.e. 152 deg) and H_∞=57 km. Results for Zeldovich reaction mechanism.

In particular, the differences between green and blue lines, on the capsule afterbody, underline that at M_∞=19 the pitching moment coefficient is affected by the chemical kinetics while no influences are expected when capsule is flying at M_∞=16 (see Fig. 18).

As far as the effect of reaction mechanism is concerned, using the Zeldovich model, the sonic line at M_∞=19 compares to that of complete reaction mechanism, as summarized in Fig. 20. As one can see, the sonic line as computed for Zeldovich model differs only

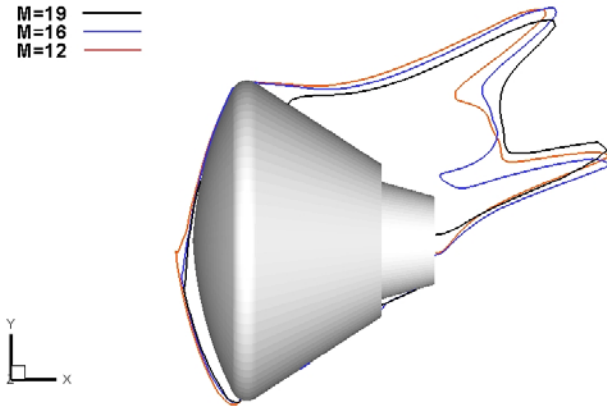slightly from that of the complete reactions mechanism.

Figure 21. Sonic line location in the capsule pitch plane at AoA=28 deg and H_∞=57 km. Comparison between M_∞ =12,16 and 19. Reacting gas computations.

Figure 21 shows the sonic line for the CRV for different Mach number (M_∞=12, 16, and 19) at the same AoA (i.e. 28 deg) thus appreciating the effect of Mach number. Therefore, region of vehicle static instability could be expected during reentry, depending on the capsule cg location.

9 CRV Aerodynamic Features

Of primary interest for an axisymmetric capsule are lift (C_L), drag (C_D), and pitching moment (C_{My}) coefficients, which are calculated using the following reference parameters:
1) 5.0 [m] (capsule diameter) as longitudinal reference length;
2) 19.6 [m^2] as reference surface;
3) pole coordinates for the pitching moment are (1.3, -0.1765, 0) [m] (vehicle cg).
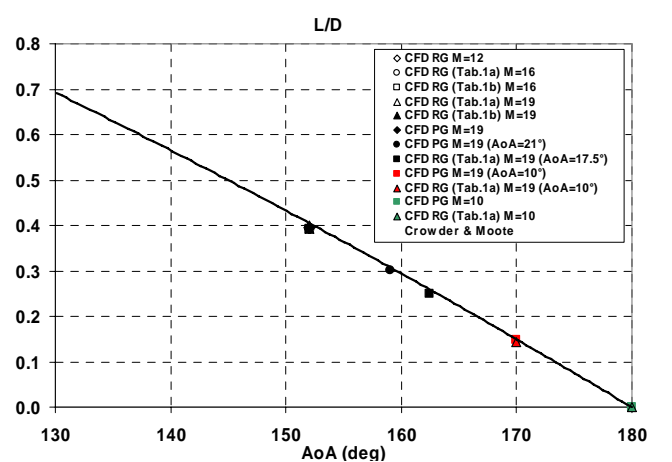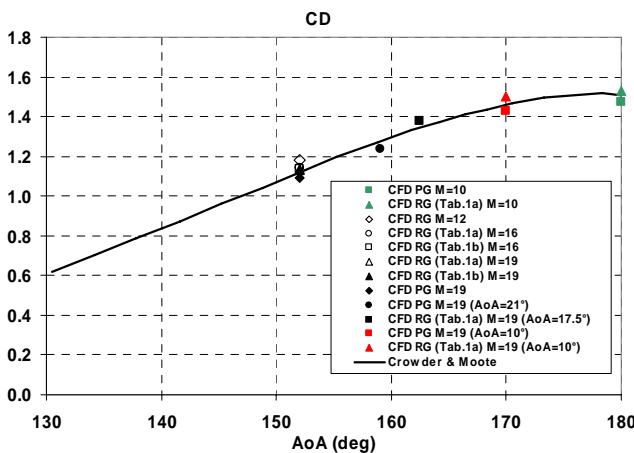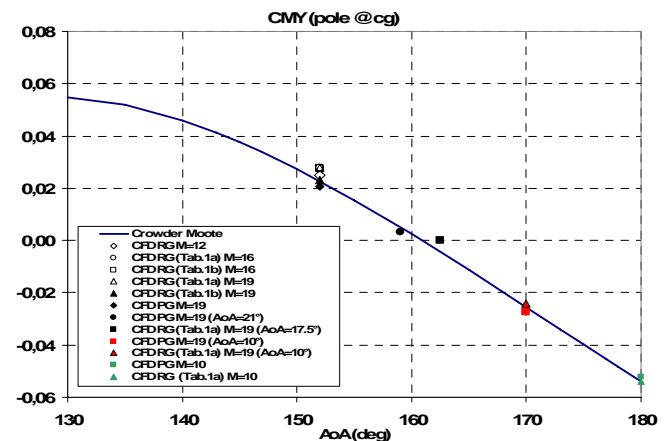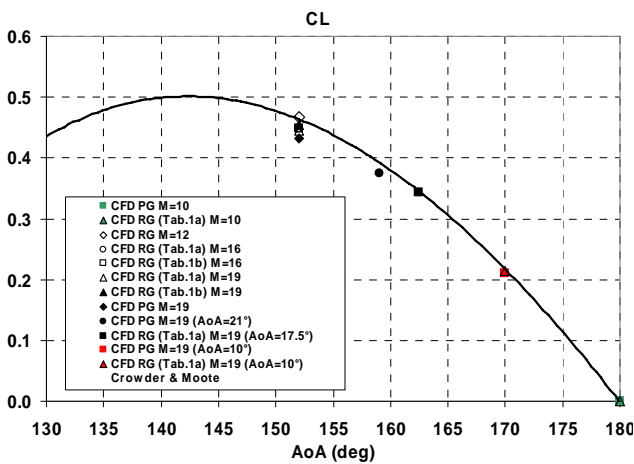

Figure 22. Lift and drag coefficients versus AoA. Comparison between present and literature data [12,20].

Figure 23. L/D ratio and pitching moment coefficients versus AoA. Comparison between present and [12,20].

The aerodynamic data set has been generated for the following ranges:
1) $3 < M < 24$ [3, 4, 8, 12, 16, 20, 24];
2) $130° < \alpha < 180°$ [130÷180]
3) $10^5 < Re < 10^7$ [0.1, 0.5, 1, 5, 10] x 10^6;
No lateral directional analysis has been taken into account in this work.

The curves of lift, drag, pitching moment coefficients and aerodynamic efficiency, are shown in Figures 22-23. Other numerical data, provided in Ref. [12, 20], are also reported to highlight accuracy of results. The CRV aerodynamics is also summarized in Table 4 where the results involve both Dunn-Kang and Park chemical kinetic models. Note that, C_{MY}, shows that the pitching moment derivative $C_{M\alpha}$ is negative in the AoA range of 150-180 deg, signifying that the CRV is statically stable for this range of AoA (provided that the capsule cg is close to the moment reference point).
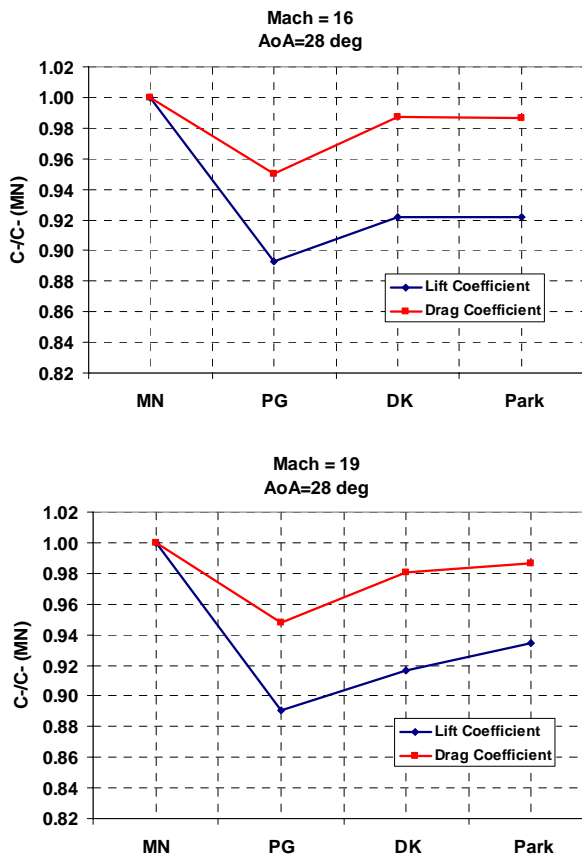
For what concerns the effect of chemical kinetics, Figures 24-25 highlight that at $M_\infty=16$ no differences are expected for aerodynamic forces, passing from Dunn-Kang to Park kinetics. On the contrary at $M_\infty=19$, both lift and drag coefficient increase ranging from PG through DK and Park kinetics. Differences of about 2 % and 5 % are observed concerning the value of C_L and C_{MY}, respectively. These conclusions for $M_\infty=19$ are confirmed by Fig. 25, where is recognized the abscissa of vehicle centre-of-pressure (x_{cp}) nondimensionalized with respect to its value for MN [12]. The increase in Cp at the stagnation region and its decrease over the remaining region lead to a forward (toward nose) shift of centre-of-pressure, or equivalently, positive (nose-up) pitching moment, as the flow γ decreases.

Figure 25 shows that at $M_\infty=16$, the x_{cp} in the case of PG solution decreases of about 10% with respect to the MN estimation and there are no differences between the values provided by both the chemical models.

Figure 24. Effect of chemical reactions at AoA= 28 deg for $M_\infty=16$ and $M_\infty=19$. Comparison among MN, PG, Dunn-Kang and Park computations.

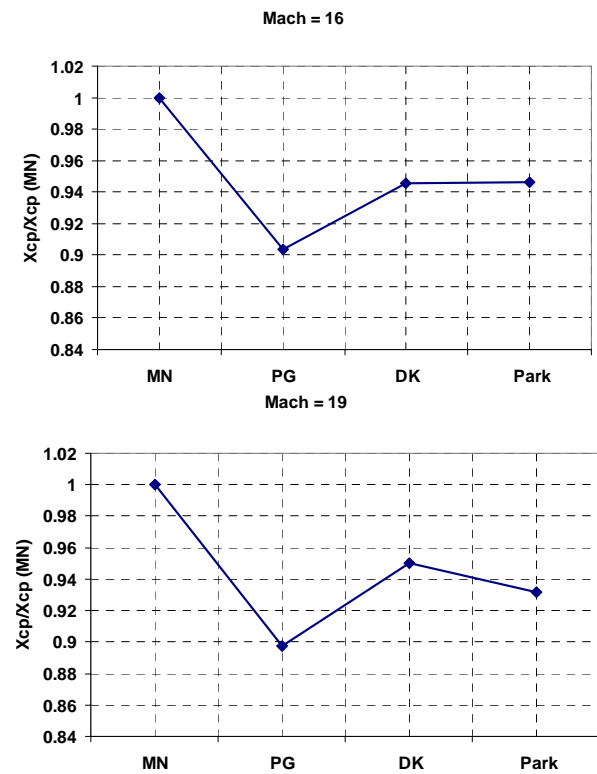**Figure 25.** Effect of chemical reactions on Xcp at AoA= 28 deg for $M_\infty=16$ and $M_\infty=19$. Comparison among MN, PG, Dunn-Kang and Park computations.

At $M_\infty=19$, instead, even if the value of x_{cp} in the case of PG solution decreases again of about 10% with respect to the MN estimation, the two chemical models provide values that differ each other of about 2%.

Note that the latter difference may be dangerous if neglected when designing vehicle thermal shield layout. Analyses of effect of chemical kinetics on capsule aerodynamics at AoA= 28 deg versus Mach number, can be found in Ref. 12.

Finally, Fig. 26 shows the effects of reaction mechanism on CRV aerodynamics when capsule is flying at AoA=28 deg, $M_\infty=19$ and H=57 km. Fig. 26 highlights, in a step-by-step approach, the effect of each reaction of reaction mechanism. As one can see, results for Zeldovich model compares globally well with those of the complete reaction mechanism, i.e. 17 reactions.
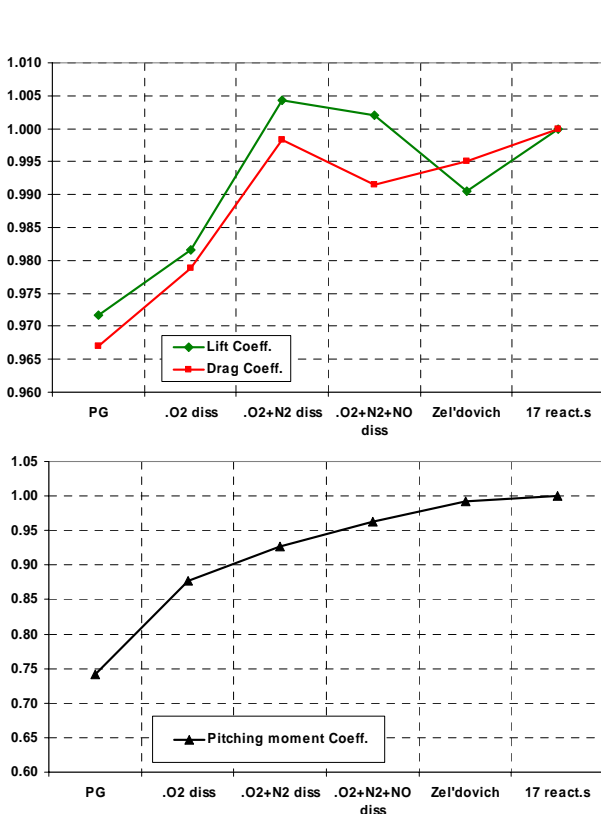
10 CRV Aerothermodynamic Features

The CRV aeroheating presents two critical regions onto the vehicle heat shield. They are the heat shield stagnation point (capsule flying at AoA=0 deg) and the vehicle side corner (capsule flying at AoA≠0 deg) [21,22,23].
Several Navier-Stokes computations have been performed assuming chemically reacting gas model, considering alternatively the heat shield surface as NC, PC and FC wall. The computations refer to fully laminar non-equilibrium flow conditions with capsule surface temperature fixed at 300 K or in radiative equilibrium conditions. Note that, due to relatively low entry velocities (e.g. no radiation heat flux applies) only convective heat flux are taken into account; moreover no heat shield ablation and recession were assumed for simplicity.
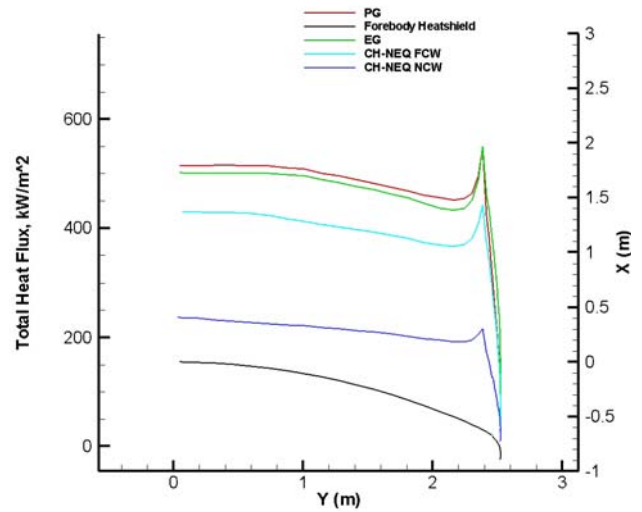
Figure 27. High temperature air effect on capsule forebody total heat flux at AoA= 0 deg, $M_\infty=19$ and $H_\infty=57$ km. $T_w=300$ K.

Figure 26. Effects of reaction mechanism on CRV aerodynamics at AoA=28 deg (i.e. 152 deg), $M_\infty=19$ and $H_\infty=57$ km.

To illustrate the high temperature real gas effects in air, Fig. 27 shows the comparison of heat flux on the forebody centerline, between the case of PG, EG and chemical non-equilibrium gas; for this latter case, the results for NCW and FCW are also reported. All these heat flux profiles are evaluated for cold wall conditions (e.g. $T_w=300$ K).

As one can see, the wall heat flux is higher in the case of chemical equilibrium condition and it is closer to the heat flux for PG simulation. This can be explained considering that as the wall is cold, the chemical equilibrium leads to the recombination of dissociated atoms.

When the boundary layer (BL) is in chemical nonequilibrium, CFD simulations confirm that the higher heat flux is attained for FCW. As shown, this value is lower than that for EG, but is very large compared with the case of NCW, as expected. Therefore, we can conclude that if the gas in the boundary layer is in equilibrium (e.g. fast recombination) then a surface catalyst will not have any effect on the formation of molecules.
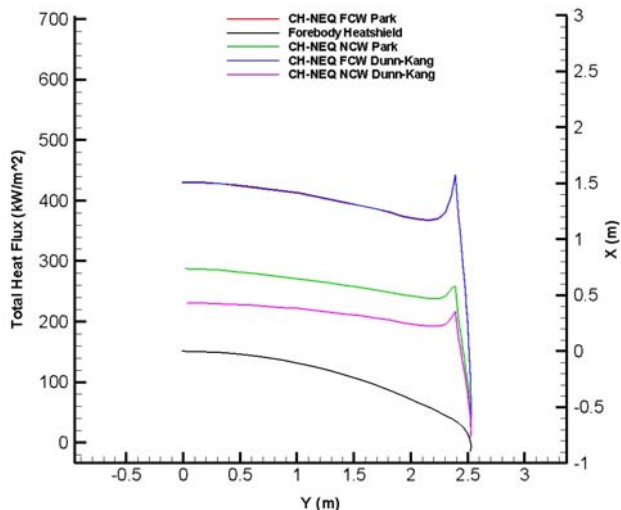

Figure 28. Effect of chemical kinetics on capsule forebody total heat flux at AoA= 0 deg , M_∞=19 and H_∞=57 km for T_w=300 K.

In this case, in fact, atoms recombine and liberate their energy of dissociation to the gas in the BL yet. This added heat tends to increase the heat flux to the surface via thermal conduction, thus concluding that the recombination of atoms is more important than in the case of a FCW.

For this reason, we regard the equilibrium condition as the reference condition in much of the state of the art TPS design activities.

As far as effect of chemical kinetics is concerned, Fig. 28 shows that in the case of a FCW a large part of $\dot{q}_c$ is due to the energy released by the recombination of atoms so that the influence of chemical kinetics is small. On

the contrary the differences in the heat flux profile, as evaluated for NCW, underline that the role of reaction rate may be very important in order to assess vehicle aerodynamic heating. Therefore, we can conclude that the chemical model are negligible for a catalytic wall and are significant in the noncatalytic case. Of course the latter conclusion is expected depending on freestream conditions.

At high altitude the shock layer has not dissociated because the shock layer is tenuous since pressure and density are low. Therefore, the number of particle collisions is low so that the chemical reactions are not much activated (e.g. the flow is nearly frozen): there is not much energy involved in dissociation. Most of the energy is in translational modes. As flying altitude decreases the density suddenly increases and the chemical reactions are activated. At very low altitude, the shock layer is so dense that the boundary layer is close to equilibrium and the atoms recombine in the boundary layer before they have a chance to strike the wall. Hence the BL is heated and there is more potential for heat transfer by conduction (e.g. reactions rate comeback to have a little effect).
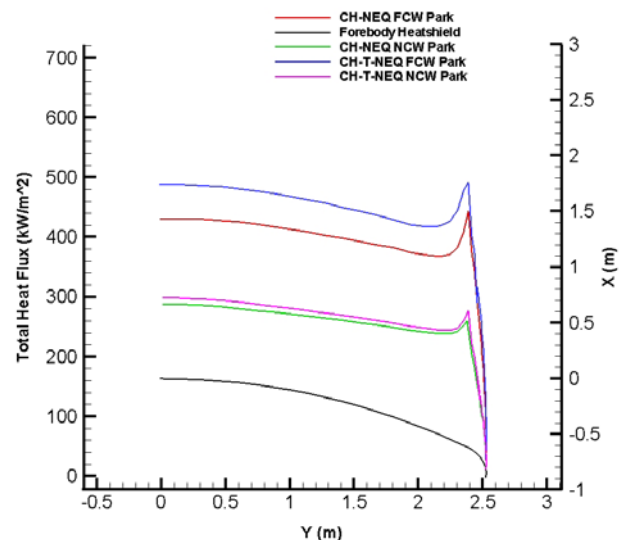

Figure 29. Effect of vibrational relaxation on capsule forebody total heat flux at AoA= 0 deg, M_∞=19 and H_∞=57 km for T_w=300 K.

Figure 29 displays, instead, the effect of vibrational relaxation on the wall heat flux. As one can see, the heat flux profile in the case of

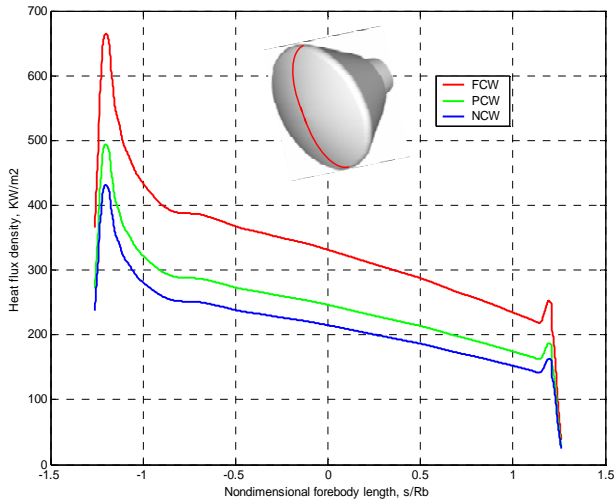FCW conditions depends on vibrational relaxation more than in the case of NCW.

Figure 30. Heat flux on the forebody OML. Nondimensional surface distance measured from centerline. Lifting trajectory. Vehicle trimmed at AoA=20 deg.
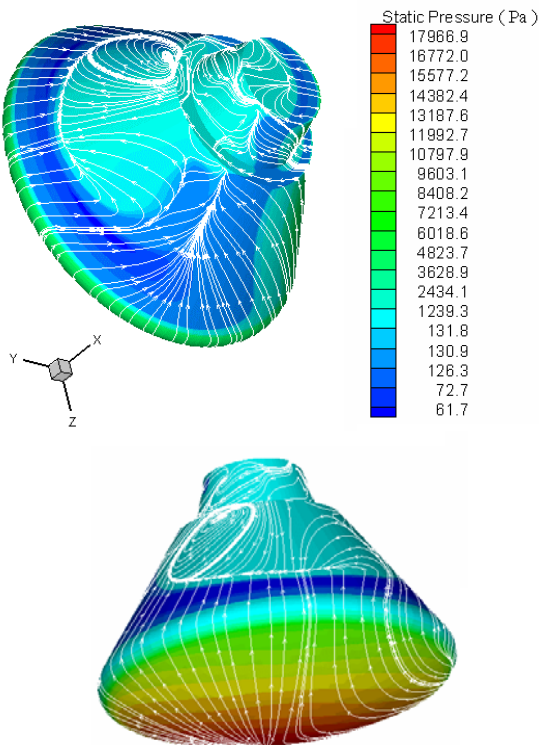

Figure 31. Pressure distribution and vehicle surface flow patterns. M_∞=19, AoA=20 deg and H=57 km. Reacting gas computation.

In order to illustrate the magnitude of the effects of catalytic activity on TPS, Fig. 30 shows the comparison of the heat flux along the forebody centreline at wall radiative equilibrium conditions, among the cases of a FC, PC and NC wall, in the case of lifting reentry (3D computations).

As one can see, the overheating caused by the catalytic action is potentially very large compared with the case of NCW. In particular, the largest difference occurs at the sphere-cone junction (corner fillet) where large changes in the flow gradients along the surface occur. Therefore the corner radius is the dominant geometric feature for the convective heating (instead of heat shield radius of curvature). Therefore it is confirmed that significant reduction in convective heat flux occurs if the thermal shield is built with a non-catalytic TPM. Finally, Fig. 31 shows the skin friction line patterns both on the capsule leeside and windside. Static pressure contours are reported with surface streamlines that highlight the complexity of the flow structure of vehicle afterbody. As one can see, the flow remains attached on the windward side of the conical afterbody, while separation occurs near the maximum diameter point on the capsule shoulder. It should be noted that the knowledge of this point is then relevant for the vehicle afterbody heating assessment. As one can see the separated zone on the capsule leeside is highlighted.

11 Conclusions

Real gas effects on the design of a Crew Return Vehicle for International Space Station have been taken into account. CFD analyses have been made to simulate the reentry of an Apollo-shaped capsule in order to determine the effect of thermal and chemical nonequilibrium on flowfield past the vehicle. Numerical results confirm that high temperature air conditions strongly affects both aerodynamics and aerothermodynamics of capsule. In particular, a comparison is made between CFD computations for perfect gas and reacting gas mixture, in order to bring into evidence the effects of finite rate chemistry, the role of reaction mechanism

with the related chemical kinetics and, finally, the influence of wall catalyticity. Model simplification is also investigated by considering a restricted set of predominant chemical reactions as Zeldovich model. Results comparisons for CRV aerodynamics confirm the strong effect of the real gas behavior on the capsule static stability. Finally, the work underlines that the exact prediction of the heat transfer and chemical environment is crucial for the design of the vehicle TPS. In fact, the possibility of reducing the heat loads on the surface of space vehicles has been highlighted.

References

[1] Sarma, G S R. Aerothermochemistry for Hypersonic Technology. VKI Lecture series 1995-04. April1995.

[2] Hassan B, Candler G V, and Olynick, D. Thermo-Chemical Nonequilibrium Effects on the Aerothermodynamics of Aerobraking Vehicles. *Journal of Spacecraft and Rockets* **30** (6), 1993.

[3] Scott C D. The Effects of Thermochemistry, Nonequilibrium, and Surface Catalysis in the Design of Hypersonic Vehicles. 1th Joint Europe-US Short Course on Hypersonic. GAMNI-SMAI. Paris, France Dec 7-11, 1987.

[4] Inger, G R: Nonequilibrium Hypersonic Stagnation Flow with Arbitrary Surface Catalycity Including Low Reynolds Number Effects. Int. J. Heat and Mass Transfer. Vol. 9, 1966, pp. 755-772.

[5] Anderson L A. Effects of Surface Catalytic Activity on Stagnation Heat Transfer Rates. *AIAA Journal* **11** (5), 1973.

[6] Anderson J D. *Hypersonic and High Temperature Gas Dynamics.* McGraw-Hill Book Company, New York, 1989.

[7] Bertin J J. *Hypersonic Aerothermodynamics.* AIAA Education series, Washington, 1994.

[8] Viviani A, Pezzella G, Cinquegrana D. Aerothermodynamic Analysis of an Apollo-like Reentry Vehicle. *Proceedings of the 14th AIAA/AHI Space Planes and Hypersonic Systems and Technologies Conferences*; 6-9 November 2006, Canberra (AU); paper AIAA-2006-8082.

[9] Pezzella G, et al. Hypersonic Aerothermal Environment Preliminary Definition of the CIRA FTB-X Reentry Vehicle. *Proceedings of the West-East High Speed Flow Field Conferences*; 19-22 November 2007, Moscow, RUSSIA.

[10] Olynick D. Trajectory-Based Thermal Protection System Sizing for a n X-33 Winged Vehicle Concept. *Journal of Spacecraft and Rockets*, **35**, (3), May-June 1998.

[11] Prabhu D K. System Design Constraints-Trajectory Aerothermal Environments. RTO AVT/VKI Lecture Series in *Critical Technologies for Hypersonic Vehicle Development*, 10 to 14 May 2004.

[12] Viviani A, Pezzella G, Borrelli S. Effect of Finite Rate Chemical Models on the Aerothermodynamics of Reentry Capsules. *Proceedings of the 15th AIAA Space Planes and Hypersonic Systems and Technologies Conferences*; 28 April-1 May 2008, Dayton (OH); paper AIAA-2008-2668.

[13] AGARD-LS-42-Vol.1, *Aerodynamic Problems of Hypersonic vehicles.* 1972.

[14] Park C, Lee Seung-Ho. Validation of Multi-Temperature Nozzle Flow Code Noznt. *Proceedings of the 28th AIAA Thermophysics Conferences*; 6-9 July 1993, Orlando (FL); paper AIAA-93-2862.

[15] Gnoffo P A, Weilmuenster K J et al. Computational Aerothermodynamic Design Issues for Hypersonic Vehicles. *Journal of Spacecraft and Rockets,* **36** (1), pag. 21-43. 1999.

[16] Gnoffo P A, Gupta R N, Shinn J. Conservation Equations and Physical Models for Hypersonic Air Flows in Thermal and Chemical Nonequilibrium. NASA TP 2867, Feb. 1989.

[17] Roe PL. Characteristic based schemes for the Euler equations. *Annual Review of Fluid Mechanic;* **18**:337-365, 1986.

[18] Walpot L, Numerical Analysis of the ARD Capsule in S4 Wind Tunnel. ESA SP.487

[19] Olynick D P, Hassan H A. New Two-Temperature Dissociation Model for Reacting Flows. Journal of Thermophysics and Heat Transfer. Vol. 7, No.4, Oct-Dec. 1993.

[20] Crowder R S, Moote J D. Apollo Entry Aerodynamics. *Journal of Spacecraft and Rockets,* **6** (3), 1969.

[21] Park C, Yoont S. Calculation of Real-Gas Effects on Blunt body Trim Angles. *AIAA Journal* **30** (4), 1992.

[22] Viviani A, Pezzella G. Catalytic Effects on Non-Equilibrium Aerothermodynamics of a Reentry Vehicle. *Proceedings of the 45th AIAA Aerospace Sciences Meeting and Exhibit*; 8-11 January 2007, Reno, NE (USA); paper AIAA-2007-1211.

[23] Viviani A, Pezzella G. Influence of Surface Catalyticity on Reentry Aerothermodynamics and Heat Shield. *Proceedings of the 39th AIAA Thermophysics Conference*; 25-28 June 2007, Miami, FL (USA); paper AIAA-2007-4047.

Table 1a. Reaction rate parameters in Eq. (21), Dunn & Kang model, Ref. 8

No	Reaction	$A_{f,r}$ (m³/kgmole s)	$\overline{T}$ (k)	$\beta_{f,r}$	$E_{af,r}$ (J/kgmole)	Third body efficiency
1	$O_2 + M = 2O + M$	3.60x10¹⁵	T	-1.0	4.947x10⁸	O₂=9, N₂=2, O=25,N=NO=1
2	$N_2 + M = 2N + M$	1.90x10¹⁴	T	-0.5	9.395x10⁸	O₂=1, N₂=2.5, O=N=NO=1
3	$N_2 + N = 3N$	4.085x10¹⁹	T	-1.5	9.395x10⁸	-
4	$NO + M = N + O + M$	3.90x10¹⁷	T	-1.5	6.277x10⁸	O₂=N₂=1, O=N=NO=20
5	$NO + O = O_2 + N$	3.20x10⁶	T	1.0	1.638x10⁸	-
6	$N_2 + O = NO + N$	7.00x10¹⁰	T	0.0	3.159x10⁸	-

Table 1b. Reaction rate parameters in Eq. (21), Park model, Ref. 9

No	Reaction	$A_{f,r}$ (m³/kgmole s)	$\overline{T}$ (k)	$\beta_{f,r}$	$E_{af,r}$ (J/kgmole)	Third body efficiency
1	$O_2 + M = 2O + M$	1.00x10¹⁹	T_a	-1.5	4.947x10⁸	O₂=N₂=NO=0.2, O=N=1
2	$N_2 + M = 2N + M$	3.00x10¹⁹	T_a	-1.6	9.412x10⁸	O₂=N₂=NO=0.233, O=N=1
3	$NO + M = N + O + M$	1.10x10¹⁴	T_a	0.0	6.277x10⁸	O₂=N₂=0.05, O=N=NO=1
4	$NO + O = O_2 + N$	2.40x10⁶	T	1.0	1.598x10⁸	-
5	$N_2 + O = NO + N$	1.80x10¹¹	T	0.0	3.193x10⁸	-

Table 2. ONERA S4 exit conditions, Ref. 18

P_0 (bar)	85	25
T_0 (k)	1151	1108
Re_D	967237.3	319208
M	9.92	9.72
P (Pa)	211.3	71.17
T (k)	55.7	55.7
T_{wall} (k)	300	300
Xcg/D	0.26	0.26
Ycg/D	0.0353	0.0353
AoA (deg)	-20	-20

Table 3. Freestream conditions of CFD computations.

Altitude (Km)	Mach (-)	Pressure (Pa)	Temperature (k)	AoA (deg)
50	10	79.78	270.65	0
57	19	32.78	255.27	10
57	19	32.78	255.27	17.5
57	19	32.78	255.27	21
57	19	32.78	255.27	28
57	16	32.78	255.27	28
57	12	32.78	255.27	28

Table 4. CRV Aerodynamics.

Mach	Flow model	AoA	C_D	C_L	L/D	C_{MY} (pole @ nose)
10	PG*	180	1.4760	0.0000	0.0000	-0.0521
	RG* (Tab. 1a)		1.5300	0.0000	0.0000	-0.0539
12	RG (Tab. 1a)	152	1.1814	0.4664	0.3948	0.0248
16	PG	152	1.0965	0.4339	0.3957	0.0212
	RG (Tab. 1a)		1.1392	0.4479	0.3932	0.0277
	RG (Tab. 1b)		1.1389	0.4480	0.3934	0.0276
19	PG	170	1.4300	0.2104	0.1471	-0.0274
	RG(Tab. 1a)		1.5000	0.2143	0.1429	-0.0240
19	PG	159	1.2400	0.3750	0.3024	0.0034
	RG(Tab. 1a)	162.5	1.3800	0.3437	0.2491	0.0001
19	PG	152	1.0940	0.4328	0.3956	0.0206
	RG (Tab. 1a)		1.1315	0.4456	0.3938	0.0278
	RG (Tab. 1b)		1.1386	0.4541	0.3988	0.0233

Copyright Statement